Electrochemical Fields within 3D Reconstructed Microstructures of Mixed Ionic and Electronic Conducting Devices

Yanxiang Zhang,[a, b, 1]* Yu Chen,[b, c, 1] Ye Lin,[b, 1] Mufu Yan,[a] William M. Harris,[d] Wilson K. S. Chiu,[d] Meng Ni,[e] Fanglin Chen[b]*

[a] National Key Laboratory for Precision Hot Processing of Metals, School of Materials Science and Engineering, Harbin Institute of Technology, Harbin 150001, China

[b] Department of Mechanical Engineering, University of South Carolina, SC 29205, USA

[c] Center for Innovative Fuel Cell and Battery Technologies, School of Materials Science and Engineering, Georgia Institute of Technology, GA 30332-0245, USA

[d] Department of Mechanical Engineering, University of Connecticut, Storrs, CT 06269,USA

[e] Building Energy Research Group, Department of Building and Real Estate, The Hong Kong Polytechnic University, Hung Hom, Kowloon, Hong Kong, China

* Authors to whom correspondence should be addressed:

Tel: +86 451 86418617, fax: +86 451 86413922, E-mail address: hitzhang@hit.edu.cn (Y. Zhang); Tel: +1 803 777 4875, fax: +1 803 777 0106, E-mail: chenfa@cec.sc.edu (F. Chen).

[1] These authors contribute equally to this work.

Abstract

The performance and stability of the mixed ionic and electronic conducting (MIEC) membrane devices, such as solid oxide cells (SOCs) and oxygen separation membranes (OSMs) interplay tightly with the transport properties and the three-dimensional (3D) microstructure of the membrane. However, development of the MIEC devices is hindered by the limited knowledge about the distribution of electrochemical fields within the 3D local microstructures, especially at surface and interface. In this work, a generic model conforming to local thermodynamic equilibrium is developed to calculate the electrochemical fields, such as electric potential and oxygen chemical potential, within the 3D microstructure of the MIEC membrane. Stability of the MIEC membrane is evaluated by the distribution of oxygen partial pressure. The cell-level performance such as polarization resistance and voltage vs. current curve can be further calculated. Case studies are performed to demonstrate the capability of the framework by using X-ray computed tomography reconstructed 3D microstructures of a SOC and an OSM. The calculation method demonstrates high computational efficiency for large size 3D tomographic microstructures, and permits parallel calculation. The framework can serve as a powerful tool for correlating the transport properties and the 3D microstructure to the performance and the stability of MIEC devices.

1. Introduction

Mixed ionic and electronic conductors (MIECs) have been widely used as the functional components of various electrochemical devices, such as solid oxide fuel cells (SOFCs) [1], solid oxide electrolyzer cells (SOECs) [2], and oxygen separation membranes (OSMs) [3]. The transport properties (e.g., ionic and electronic conductivities and surface exchange coefficients) and the three-dimensional (3D) microstructure of MIECs in these devices play critical roles in determining the performance and stability. The transport processes within the SOFCs, SOECs, and OSMs membranes are essentially: 1) the transport of oxygen ions within the MIEC bulk, 2) the transport of electrons within the MIEC bulk, 3) the surface exchange of oxygen molecules at the MIEC surface, 4) the charge transfer of oxygen ions and electrons across the MIEC interface, and 5) gas transport within the pores if any. Electrochemical fields such as oxygen chemical/electrochemical potential, electrostatic/electric potential, ionic and electronic current densities may vary significantly across micro/nano-scale features, such as surfaces and interfaces. This is particularly obvious for many MIEC materials whose conductivity is dominated by either oxygen ions or electrons, for example yttria-stabilized zirconia (YSZ), gadolinia-doped ceria (GDC), Sr-doped $LaMnO_3$ (LSM), etc. The electrochemical reaction for these MIECs is constrained to the three-phase boundary (TPB) where the surface meets with the interface. The reaction zone extends to the MIEC surface when the MIEC for example $(La,Sr)(Co,Fe)O_3$ (LSCF) has pronounced conductivities of both oxygen ions and electrons [4]. For the rational design of these MIEC membranes, it is essential to understand how the transport properties and 3D microstructures affect the performance. However, this is still challenging because the pronounced interplay between MIEC properties and 3D microstructures is complex. Many theoretical models have been developed to correlate MIEC properties and 3D

microstructures to the performance of MIEC devices, for instance the electrode polarization resistance models based on porous electrode theory [5-7], and the multi-physics models based on averaged microstructures [8-10]. However the validity of these models is limited by MIEC properties and operation conditions. In addition, difficulties in eliminating the uncertainty of averaged microstructure factors raise critical concerns about the prediction accuracy. Thus, the microstructure - performance relationship is understood mostly in an empirical way. So far, it is not clear about the degree to which the performance of SOFCs, SOECs, or OSMs can be further enhanced by microstructure optimization. Compared with the continuum models based on immeasurable parameters (chemical potentials of electrons and oxygen ions, and electrostatic potential) [11, 12], a model based on measurable parameters (chemical potential of O_2 and electric potential) is more useful from an experimental standpoint. Especially, the models solving numerically the simple governing equations for the transport processes with the complex 3D microstructures of the MIEC device could show a unique capability of studying the electrochemical field distributions within the 3D local microstructures (e.g. surface and interface) and correlating materials properties and 3D microstructures with performance in an unambiguous manner.

The 3D imaging of microstructures by X-ray computed tomography (XCT) and focused ion-beam (FIB) serial sectioning permits the calculation of the multi-physics with the reconstructed 3D structures [13], and thus the accurate microstructure - performance relationship. To this end, several attempts have been made on an electrode level. For instance the Ni-YSZ electrode, the multi-physics including the transport of ions within YSZ, transport of electrons within Ni, charge transfer at TPB, and gas diffusion within pores have been calculated by finite volume method (FVM) [14], and lattice Boltzmann method [15, 16]. The MIEC air

electrodes such as LSCF [17-20] and LSM [21] have also been studied by incorporating governing equations of ions transport and surface exchange into the 3D reconstruction microstructures. However, all the above-mentioned models consider only one charge carrier, while neglecting the others to calculate charge transport within each individual phase, especially within the electrolyte. The thermodynamic analysis by Virkar suggests that the transport of both electrons and oxygen ions should be considered, so that the formulation is in consistent with the postulation of local thermodynamic equilibrium and the oxygen chemical potential within MIECs concerning the stability can be calculated correctly [22, 23]. Combining with the transport of electrons and ions within each phase, a complete formulation can be achieved by choosing a proper description of the oxygen surface exchange on the surface of each phase. The transport of ions and electrons as well as surface exchange has been characterized by well-defined properties, such as ionic and electronic conductivities, and surface exchange coefficient. Although the transport properties for many MIECs have been reported by a huge volume of studies, such a complete formulation using electronic conductivity, ionic conductivity and surface exchange coefficient of each phase of the MIEC device has never been used. Idealizations beyond irreversible thermodynamics, such as purely ionic conduction of electrolyte, uniform Fermi level (electrochemical potential of electrons) within predominantly electronic conductors and equilibrium state of surface exchange are usually used to obtain mathematically accessible solutions. These idealizations however challenge the postulations of steady-state thermodynamics, such as the existence of local equilibrium and the thermodynamic equation of motion. Thus, it is misty how the materials properties correlate to performance and stability. Accordingly, the quantitative linkage between the materials properties, 3D microstructures and

performance is urgently needed in this regard. Actually, such a complete formulation is universal to SOFCs, SOECs, and OSMs on a cell level.

In this study, we have developed a complete formulation based on linear non-equilibrium thermodynamics for the transport of ions and electrons, and surface exchange within the 3D microstructure of MIEC membrane. The calculation of the multi-physics within the 3D MIEC microstructure is accomplished by home-built Matlab codes. The computational framework is dedicated to calculating the distributions of experimentally measurable variables, including electric potential and chemical potential of oxygen within the 3D microstructure. Post-processing permits calculation of electronic/ionic current distributions, oxygen partial pressure distribution, overpotential distributions, voltage vs. current curve, oxygen permeation flux, and area specific resistance (ASR). The calculation is free from empirical/fitting parameters. All computational inputs are based on well-studied properties which can be measured by well-established experiments. In addition, the complexity of the 3D tomographic microstructure can be substantial. For example, the membrane can contain many sub-phases and multi-layers, e.g. (porous/composite) air/fuel, electrode/electrolyte half cells, (polycrystal/composite) electrolytes, and single cells. We have also developed an effective strategy to improve the computational efficiency. The algorithm can tackle ~40 million voxels on a 16 GB RAM personal computer, while the reported domain size in the literature is $0.025 \sim 9$ million voxels, sometimes with the aid of a high performance computing cluster [14-21]. Demonstrative calculations on a cell level are conducted using the simulated microstructures of patterned LSM/YSZ/LSM symmetric cell, LSCF/YSZ/LSCF symmetric cell, the XCT reconstructed 3D microstructures of GDC-CFO ($CoFe_2O_4$) OSM, and GDC-Ni/GDC/GDC-SSC ($Sm_{0.5}Sr_{0.5}CoO_3$) SOFC/SOEC. Classic insight

is consolidated and new insight is provided into the correlation between local electrochemical field distributions and cell-level performance and stability of the MIEC devices.

2. Irreversible Thermodynamics Formulation

Although the transport equations are not entirely new, their derivations are provided here in a unified and comprehensive manner. Beginning with the Onsager equations, the transport processes within MIEC could be modeled on a basis of non-equilibrium thermodynamics. The features of this framework are summarized as follows:

1) The usage of experimentally measurable variables (oxygen chemical potential and electric potential), instead of immeasurable variables (chemical potential of ions and electro-statistic potential), so that the calculation can be easily understood in experimental perspectives.

2) The usage of local equilibrium (the cornerstone of steady-state thermodynamics) for transports with MIEC bulk. That is, both the transports of oxygen ions and electrons within each individual phase of the MIEC device are considered, so that the oxygen partial pressure within the MIEC device (especially at the vicinity of interface) can be calculated correctly. Thus, this further permits the evaluation of stability, such as the risk of oxidation/reduction of materials and the risk of cracking of interface.

3) The usage of steady-state thermodynamics for the surface exchange of oxygen. This is crucial to form a complete formulation by combining with the previous two features, making correct calculation results and permitting the use of surface exchange coefficient by well-defined experiments. In the literature, the oxygen surface exchange is usually assumed to be in thermodynamic equilibrium or be formulized by Butler-Volmer type equations, which are generally not valid since the surface exchange is sluggish and electroneutral.

2.1 Transport of charged components within solid state conductors

For general consideration, we first consider a solid state system consisting of mobile charged components. When the system is at equilibrium, the electrochemical potential of each component must be uniform throughout the entire system, and there is no net flux of species. When the system is driven away from equilibrium, there will be a spatial variation of electrochemical potentials and thus a net flux of species will occur. The transport at non-equilibrium can be formulated by irreversible thermodynamics [24]. Depending on the extent to which the system is away from equilibrium, irreversible thermodynamics can be classified into three regimes: 1) linear non-equilibrium thermodynamics for system near equilibrium; 2) Nonlinear non-equilibrium thermodynamics and 3) extended thermodynamics for system substantially away from equilibrium. It is unfortunately a rather vague wording here for this classification. But linear non-equilibrium thermodynamics may be qualified for the formulation of transport within solid state systems, since many fundamental laws subjecting to this regime have shown successful applications, for example, Fick's first law, Ohm's law, and Fourier's law. Linear non-equilibrium thermodynamics postulates linear relations between each flux and all the thermodynamic forces, given by the Onsager equations [25],

$$J_i = \sum_j L_{ij} X_j \tag{1}$$

where J_i is the flux of component i. X_j is the thermodynamic force on component j. L_{ij} is the Onsager coefficient, yielding to $L_{ij} = L_{ji}$. Allnatt derived a formula for the Onsager coefficients at an atomic level, and suggested that L_{ij} $(i \neq j)$ is zero if the moving i component does not interfere with the moving j component [26]. In most practical applications of Eq. 1, the off-diagonal terms L_{ij}'s $(i \neq j)$ are, however, discarded. The measurement of L_{ij}'s $(i \neq j)$ is still challenging, especially

for solid state transport. Although no guarantee exists that L_{ij}'s ($i \neq j$) are negligible, it is fortunate to see the good agreement with experiments without considering the coupling of thermodynamic forces. By discarding the off-diagonal terms, Eq. (1) is then simplified as,

$$J_i = L_{ii} X_i \tag{2}$$

When the fluxes are driven by electric field and chemical potential gradients, the driving forces can be given by [25],

$$X_i = -\nabla \tilde{\mu}_i \tag{3}$$

where $\tilde{\mu}_i$ is the electrochemical potential of component i. The negative sign in Eq. (3) arises because the force is in the opposite direction of the gradient of $\tilde{\mu}_i$. The electrochemical potentials are defined as,

$$\tilde{\mu}_i = \mu_i + z_i F \Phi \tag{4}$$

where μ_i is the chemical potential, z_i is the number of charges on i, F is Faraday constant, and Φ is the electrostatic potential or Galvani potential. The diagonal Onsager coefficients are thus defined as,

$$L_{ii} = U_i C_i \tag{5}$$

where C_i is the volumetric concentration of component i, and U_i is the mobility of component i, or the ratio of its particle's velocity to the thermodynamic force $-\nabla \tilde{\mu}_i$. In electrochemistry, it is interesting to note that the mobility of a charged species is defined by the ratio of its velocity to electric field $-\nabla \Phi$, and usually denoted by u_i [27]. If the fluxes are driven by electric field in the absence of chemical potential gradient, then, according to Eqs. (3, 4), we can easily deduce,

$$U_i = \frac{u_i}{z_i F} \tag{6}$$

The assumption of the absence of chemical potential gradient, though useful in the derivation of Eq. (6), does not constrain the equation's validity when chemical potential gradient also exists. Combining Eqs. (2, 3, 5, 6), we obtain,

$$J_i = -\frac{u_i C_i}{z_i F} \nabla \tilde{\mu}_i \tag{7}$$

The conductivity σ_i is related to its mobility by,

$$\sigma_i = z_i F u_i C_i \tag{8}$$

Thus, Eq. (7) can be expressed as,

$$J_i = -\frac{\sigma_i}{(z_i F)^2} \nabla \tilde{\mu}_i \tag{9}$$

According to Nernst–Einstein equation, we have,

$$\frac{\sigma_i}{D_i^\sigma} = \frac{(z_i F)^2 C_i}{RT} \tag{10}$$

where D_i^σ is called a self-diffusion coefficient or charge diffusion coefficient. But D_i^σ does not correspond to any diffusion coefficient that can actually be measured by Fick's laws. In other words, it is meaningless to directly use D_i^σ in Fick's laws. However, Eq. (9) can be still rewritten as,

$$J_i = -\frac{C_i D_i^\sigma}{RT} \nabla \tilde{\mu}_i \tag{11}$$

Any one of Eqs. (7, 9, 11) can be used to formulate the transport of charged particles within solid state conductors. The mobility, conductivity and self-diffusion coefficient depend on many factors, for example the type of lattice, the mechanism of migration, and the type of component in the matrix. But the Onsager coefficients are independent of the gradient of electrochemical potential.

2.2 Transport of O^{2-} and e^- within MIEC bulk

The MIEC conductors in this study refer to these solid state conductors whose mobile charges are both O^{2-} and e^-, with other charges virtually immobile. Examples for this material family could be the fluorite structure electrolytes and the perovskite structure catalysts for use in SOFCs, SOECs, and OSMs. Transport of O^{2-} can be accomplished by vacancy mechanism or interstitial mechanism, while transport of e^- can be accomplished by migration of itinerant electrons or polarons. According to Eqs. (9, 11), the transport of O^{2-} and e^- within MIEC bulk can be respectively given by,

$$J_{O^{2-}} = -\frac{\sigma_{O^{2-}}}{4F^2}\nabla\tilde{\mu}_{O^{2-}} = -\frac{C_{O^{2-}}D_{O^{2-}}^{\sigma}}{RT}\nabla\tilde{\mu}_{O^{2-}} \tag{12}$$

$$J_{e^-} = -\frac{\sigma_{e^-}}{F^2}\nabla\tilde{\mu}_{e^-} = -\frac{C_{e^-}D_{e^-}^{\sigma}}{RT}\nabla\tilde{\mu}_{e^-} \tag{13}$$

Instead of using electrochemical potentials, we choose chemical potential of O_2, μ_{O_2} and electric potential, φ which are experimentally measurable as the independent variables of Eqs. (12, 13). In practice, the electric potential is exactly the potential measured by instruments such as a voltmeter. The electric potential is related to the electrochemical potential of electrons through

the equation $\varphi = -\tilde{\mu}_e / F$. This equation is known as Hebb notation [28], and widely used in the literature [11, 12, 22, 23, 29]. Thus Eq. (13) can be rewritten as,

$$J_{e^-} = \frac{\sigma_{e^-}}{F} \nabla \varphi = \frac{FC_{e^-} D_{e^-}^{\sigma}}{RT} \nabla \varphi \qquad (14)$$

In order to formulate the transport of oxygen ions without using immeasurable electrostatic potential, we employ a fundamental postulation of non-equilibrium thermodynamics - the local equilibrium [22, 23]. We consider the reaction $O^{2-} \Longleftrightarrow 1/2O_2 + 2e^-$ within the bulk of materials is at local equilibrium, thus we have a balance between the electrochemical potential of O^{2-} and the chemical potential of O_2 (μ_{O2} , measurable) and electrochemical potential of e^- (-$F\varphi$, measurable). That is, $\tilde{\mu}_{O^{2-}} = \frac{1}{2} \mu_{O_2} + 2\tilde{\mu}_{e^-}$. Thus, Eq. (12) can be rewritten as,

$$J_{O^{2-}} = -\frac{\sigma_{O^{2-}}}{4F^2} \nabla \left[\frac{1}{2}\mu_{O_2} - 2F\varphi \right] = -\frac{C_{O^{2-}} D_{O^{2-}}^{\sigma}}{RT} \nabla \left[\frac{1}{2}\mu_{O_2} - 2F\varphi \right] \qquad (15)$$

The self-diffusion coefficient of O^{2-} can also be given by the ratio between the ^{18}O tracer diffusion coefficient and Haven ratio [30]. Now the transports of oxygen ions and electrons have been described by parameters that can be measured by experiments. In the operation of solid oxide devices, such as SOFCs, SOECs, and OSMs, the chemical potential of O_2 and the electric potential are actually the most important variables that can be well controlled and quantitatively imposed on the boundary of the MIEC conductor.

2.3 Heterogeneous reactions at interface

Considering a general reaction consisting of chemicals Ω_j ($j = 1, ..., n$) at the interface between phase I and phase II, the stoichiometric equation is expressed by [31],

$$\sum_{j=1}^{r} |v_j| \Omega_j \xrightarrow[k_b]{k_f} \sum_{j=r+1}^{n} |v_j| \Omega_j \qquad (16)$$
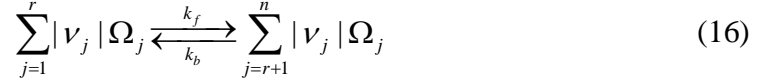
where r denotes the number of reactants, so that $n - r$ is the number of products. v_j is the stoichiometric coefficient. k_f and k_b are respectively the forward and backward rate constants of the reaction. The overall rate of the reaction may be given by the law of mass action,

$$r = k_f \prod_{j=1}^{r} [\Omega_j]^{|v_j|} - k_b \prod_{j=r+1}^{n} [\Omega_j]^{|v_j|} \qquad (17)$$

where $[\Omega_j]$ denotes the molar fraction or partial pressure of Ω_j. Eq. (17) assumes that the order of reaction with respect to each component equals to the absolute value of its stoichiometric coefficient. This is true for elementary (single-step) reactions, and even valid for some multi-step reactions. k_f and k_b can be given by transition state theory as [27],

$$k_f = A \exp\left(-\frac{\Delta G_f^{\dagger}}{RT}\right); k_b = A \exp\left(-\frac{\Delta G_b^{\dagger}}{RT}\right) \qquad (18)$$

where A is a constant. $\Delta G_f^{\dagger}$ or $\Delta G_b^{\dagger}$ is the activation energy in going from the reactants or the products to the activated complex (transition state). In a thermodynamically consistent formulation, the activation energy can be given as [32],

$$\Delta G_f^{\dagger} = \Delta G_{ts}^{ex} - \Delta G_f^{ex}; \Delta G_b^{\dagger} = \Delta G_{ts}^{ex} - \Delta G_b^{ex} \qquad (19)$$

where,

$$\Delta G_f^{ex} = \sum_{j=1}^{r} |v_j| \left(\mu_j^0 + RT \ln a_j + z_j F \Phi_j\right) \qquad (20)$$

13

$$\Delta G_b^{ex} = \sum_{j=r+1}^{n} |v_j| \left(\mu_j^0 + RT \ln a_j + z_j F \Phi_j \right) \tag{21}$$

$$\Delta G_{ts}^{ex} = \Delta G_{ts}^0 + RT \ln a_{ts} + \alpha_a \sum_{j=1}^{r} |v_j| z_j F \Phi_j + \alpha_c \sum_{j=r+1}^{n} |v_j| z_j F \Phi_j \tag{22}$$

where μ_j^0 denotes the standard chemical potential, and a_j denotes the activity coefficient. ΔG_{ts}^0 and a_{ts} are the standard free energy and activity coefficient of the activated complex. α_a and α_c are the transfer coefficients, typically holding $\alpha_a + \alpha_c = 1$. Combining Eq. (17) with Eqs. (18-22), the rate of the reaction can be expressed by,

$$r = A \exp\left(-\frac{\Delta G_{ts}^{ex} + \sum_{j=1}^{r} v_j \tilde{\mu}_j}{RT} \right) \left\{ 1 - \exp\left(\frac{\sum_{j=1}^{n} v_j \tilde{\mu}_j}{RT} \right) \right\} \tag{23}$$

Therein, the stoichiometric coefficients are positive for products, and negative for reactants. It is shown that the reaction rate is zero when the reaction is at thermodynamic equilibrium, that is $\sum_{j=1}^{n} v_j \tilde{\mu}_j = 0$. When the reaction deviates only slightly from equilibrium, linearization of Eq. (23) is feasible, given by,

$$r = -\frac{\Re_0}{RT} \sum_{j=1}^{n} v_j \tilde{\mu}_j \tag{24}$$

where $\Re_0$ is the equilibrium exchange rate of the reaction, given by $A \exp\left(-\frac{\Delta G_{ts}^{ex}}{RT} \right)$. According to conservation of charge,

$$\sum_{j=1}^{n} \nu_j z_j = \sum_{j \in \text{phase I}} \nu_j z_j + \sum_{j \in \text{phase II}} \nu_j z_j = 0 \tag{25}$$

Then we deduce,

$$\sum_{j=1}^{n} \nu_j z_j F \Phi_j = F\left(\Phi_{\text{I}} - \Phi_{\text{II}}\right) \sum_{j \in \text{I}} \nu_j z_j \tag{26}$$

If the combination of species in phase I or II is not neutral, that is $\sum_{j \in \text{I}} \nu_j z_j \neq 0$, Eq. (23) will show

Tafel-like behavior [4, 33], and $\mathfrak{R}_0$ well depends on the equilibrium electrostatic potentials of

species. If the combination of species in phase I or II is neutral, the rate equation can be

expressed as,

$$r = A \exp\left(-\frac{\Delta G_{ts}^0 + RT \ln a_{ts} + \sum_{j=1}^{r} \nu_j \mu_j}{RT}\right) \left\{1 - \exp\left(\frac{\sum_{j=1}^{n} \nu_j \mu_j}{RT}\right)\right\} \tag{27}$$

Linearization of Eq. (27) near equilibrium gives,

$$r = -\frac{\mathfrak{R}_0}{RT} \sum_{j=1}^{n} \nu_j \mu_j \tag{28}$$

$\mathfrak{R}_0$ is now independent of the electrostatic potentials of species, given by

$A \exp\left(-\dfrac{\Delta G_{ts}^0 + RT \ln a_{ts}}{RT}\right)$. In thermodynamics, $-\sum_{j=1}^{n} \nu_j \mu_j$ is defined as the affinity of the
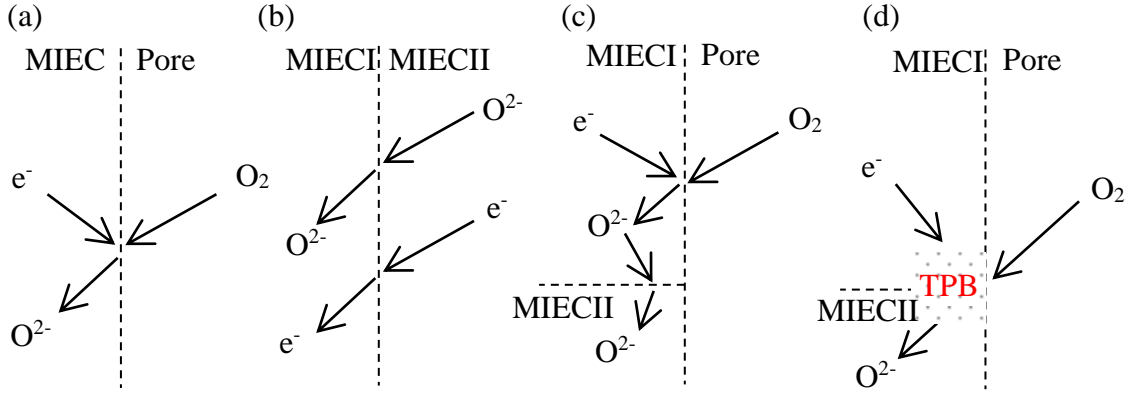
reaction [31].

Figure 1. Illustrations of surface exchange of oxygen at MIEC surface (a); charge transfer of oxygen ion and electron at MIEC interface (b); coupling of surface exchange and charge transfer at the vicinity of TPB (c); and mechanistic model of TPB with a certain thickness representing the size of reaction domain (d).

2.4 Surface exchange and charge transfer at MIEC surface and interface

The surface exchange reaction of interest is oxygen reduction reaction (ORR) at MIEC surface, $1/2O_2^{pore} + 2e^- \rightarrow O^{2-}$ as illustrated in Fig. 1a. As oxygen in the pore phase is neutral and the change of charge in MIEC phase is zero, the rate equation for ORR can be given by Eq. (27). While for the ORR near equilibrium, the rate equation of ORR, or the rate of O^{2-} generation is given by Eq. (28), namely,

$$r_{O^{2-}}^{ORR} = -\frac{\mathfrak{R}_0^{ORR}}{RT}\left(\mu_{O^{2-}} - 1/2\mu_{O_2}^{pore} - 2\mu_{e^-}\right) \tag{29}$$

In the MIEC phase just close to the MIEC/pore interface, the local equilibrium of reaction, $1/2O_2 + 2e^- = O^{2-}$ suggests $\mu_{O^{2-}} - 1/2\mu_{O_2} - 2\mu_{e^-} = 0$. Thus Eq. (29) can be expressed as,

16

$$r_{O^{2-}}^{ORR} = \frac{\Re_0^{ORR}}{2RT}\left(\mu_{O_2}^{pore} - \mu_{O_2}\right)$$ (30)

The equilibrium exchange rate $\Re_0^{ORR}$ can be further correlated to the surface exchange coefficient by electric conductivity relaxation (ECR) method, k^δ [34] or by ^{18}O tracer diffusion method, $k*$ [35]. For the two methods, thermodynamic equilibrium has been reached for the ORR reaction as the initial condition. During the ECR measurement, a new $\mu_{O_2}^{pore}$ is maintained, but not far away from its initial value, and thus the μ_{O_2} in MIEC changes gradually from the initial value to the new $\mu_{O_2}^{pore}$. The rate can be expressed by Eq. (30), which can be mathematically rewritten as,

$$r_{O^{2-}}^{ORR} = \frac{\Re_0^{ORR}}{2RT}\frac{\partial\mu_{O_2}}{\partial\ln[O^{2-}]}\frac{\partial\ln[O^{2-}]}{\partial[O^{2-}]}\left([O^{2-}]^{eq} - [O^{2-}]\right) \equiv k^\delta\left(C_{O^{2-}}^{eq} - C_{O^{2-}}\right)$$ (31)

where $[O^{2-}]^{eq}$ denotes the equilibrium molar fraction of O^{2-} in MIEC lattice corresponding to the new $\mu_{O_2}^{pore}$. Thus,

$$\Re_0^{ORR} = k^\delta C_{O^{2-}} / \gamma$$ (32)

where γ is so-called thermodynamic factor, defined by $\frac{1}{2RT}\frac{\partial\mu_{O_2}}{\partial\ln[O^{2-}]}$. While in the ^{18}O tracer diffusion experiment, $^{18}O_2$ is introduced into the pure O_2 atmosphere. Because $^{18}O_2$ and O_2 are chemically identical, the ORR reaction still maintains thermodynamic equilibrium. Thus, the net flux of oxygen ion into the MIEC is zero,

$$r_{^{18}O^{2-}}^{ORR} = -r_{O^{2-}}^{ORR} = \frac{\Re_0^{ORR}}{RT}\left(\mu_{O^{2-}} - 1/2\mu_{O_2}^{pore} - 2\mu_{e^-}\right)$$ (33)

17

The equilibrium also indicates that μ_{e^-} and the activity coefficient of O^{2-} are not changed. Thus, a new equilibrium chemical potential of O^{2-}, $\mu_{O^{2-}}^{eq}$ will build up in accordance to the new $\mu_{O_2}^{pore}$, and the change in $\mu_{O^{2-}}$ is responsible to the change in $C_{O^{2-}}$. That is,

$$r_{^{18}O^{2-}}^{ORR} = \frac{\mathfrak{R}_0^{ORR}}{RT}\left(\mu_{O^{2-}} - \mu_{O^{2-}}^{eq}\right) = \frac{\mathfrak{R}_0^{ORR}}{RT}\left(RT\ln\frac{C_{O^{2-}}}{C_{O^{2-}}^{eq}}\right) \tag{34}$$

When $C_{O^{2-}} \approx C_{O^{2-}}^{eq}$, Eq. (34) can be linearized as,

$$r_{^{18}O^{2-}}^{ORR} = \mathfrak{R}_0^{ORR}\left(\frac{C_{O^{2-}} - C_{O^{2-}}^{eq}}{C_{O^{2-}}}\right) \tag{35}$$

Because the concentration of oxygen ion, $C_{O^{2-}} + C_{^{18}O^{2-}}$ is not changed, we have,

$$r_{^{18}O^{2-}}^{ORR} = \mathfrak{R}_0^{ORR}\left(\frac{C_{^{18}O^{2-}}^{eq} - C_{^{18}O^{2-}}}{C_{O^{2-}}}\right) \equiv k^*\left(C_{^{18}O^{2-}}^{eq} - C_{^{18}O^{2-}}\right) \tag{36}$$

It leads to,

$$\mathfrak{R}_0^{ORR} = k^* C_{O^{2-}} \tag{37}$$

Another way to estimate $\mathfrak{R}_0^{ORR}$ is by AC impedance measurement. The ASR of ORR reaction on a flat surface can be given by,

$$ASR^{ORR} = \frac{\mu_{O_2}^{pore} - \mu_{O_2}}{-8F^2 r_{O^{2-}}^{ORR}} = \frac{RT}{4F^2 \mathfrak{R}_0^{ORR}} \tag{38}$$

18

The charge transfer refers to the transfer of O^{2-} or e^- across MIEC interface. The rate equation can be given by Eq. (23), and particularly given by Eq. (24) for near equilibrium. By replacing the electrochemical potentials with measurable variables (μ_{O_2} and φ), the rate equations for charge transfer of O^{2-} and e^- from MIEC II to MIEC I (Fig. 1b) can be given respectively by,

$$r_{O^{2-}}^{CT} = \frac{\mathfrak{R}_0^{CT,O}}{RT}\left[\frac{1}{2}\left(\mu_{O_2}^{II} - \mu_{O_2}^{I}\right) - 2F\left(\varphi^{II} - \varphi^{I}\right)\right] \tag{39}$$

$$r_{e^-}^{CT} = \frac{-F\mathfrak{R}_0^{CT,e}}{RT}\left(\varphi^{II} - \varphi^{I}\right) \tag{40}$$

The equilibrium rate of charge transfer, $\mathfrak{R}_0^{CT}$ can be correlated to the charge transfer resistance, ASR^{ct} that may be measurable by AC impedance under open circuit. For charge transfer of O^{2-} near equilibrium, the electric potentials are not driven far from equilibrium values, $\varphi^{I,eq}$ and $\varphi^{II,eq}$, yielding $\frac{1}{2}\left(\mu_{O_2}^{II} - \mu_{O_2}^{I}\right) - 2F\left(\varphi^{II,eq} - \varphi^{I,eq}\right) = 0$. If we postulate that the chemical potential of electrons does not change during impedance measurement, that is φ - Φ is constant, the overpotential, η yields $\varphi^{II} - \varphi^{I} = (\varphi^{II,eq} - \varphi^{I,eq}) + \eta$. According to Eq. (39), we have,

$$ASR_{O^{2-}}^{CT} = \frac{\eta}{-2Fr_{O^{2-}}^{CT}} = \frac{RT}{4F^2\mathfrak{R}_0^{CT,O}} \tag{41}$$

For charge transfer of e^- near equilibrium, we have $\varphi^{II} - \varphi^{I} = \eta$, and thus,

$$ASR_{e^-}^{CT} = \frac{\eta}{-Fr_{e^-}^{CT}} = \frac{RT}{F^2\mathfrak{R}_0^{CT,e}} \tag{42}$$

In general, the charge transfer resistance is not detectable in the Nyquist plot of impedance [5]. Although negligible, the charge transfer resistance may be quantified using high frequency resolution method, such as distribution of relaxation time of impedance [36]. But it seems rational to assume the charge transfer is facile under typical conditions.

The ORR reaction may interfere with charge transfer of O^{2-} and e^-. The coupling is strong when they occur at the vicinity of the three phase boundary (TPB), where pore, MIEC I and MIEC II connect with each other. As shown in Fig. 1c, the ORR reaction at pore/MIEC I surface produces O^{2-} first. Then O^{2-} transports to the MIEC I/MIEC II interface within MIEC I. Finally, O^{2-} transfers across the interface into MIEC II. This is one possible path out of many possibilities. The surface exchange couples tightly with the charge transfer process, when the surface exchange and the charge transfer are constrained at the TPB. One example is the porous LSM electrode on YSZ electrolyte, where LSM is predominantly electronic conductor and YSZ is predominantly ionic conductor [6]. It should be noted that the concept of TPB by this philosophy is not a line, but a region with a certain thickness, as shown in Fig. 1d. The thickness of TPB represents the size of reaction zone. In general, the reaction zone tends to be smaller with the increase of equilibrium rate of ORR, $\Re_0^{ORR}$ and with the decrease of ionic conductivity, $\sigma_{O^{2-}}$ or electronic conductivity, σ_{e^-} [37]. Some mechanistic models simplified the kinetics of the coupling of ORR and charge transfer as a Butler-Volmer rate expression normalized by TPB length. Sometimes, the TPB is considered to have a bulk resistivity or resistance per length [6, 38]. Although simple, these models are essentially simplified versions of the coupling of surface exchange and charge transfer process and even the bulk transport. Another phenomenological model is the 'direct TPB reaction' [39]. That is, O_2 in the pore combines with e^- in MIEC I and produces O^{2-} in MIEC II. This reaction occurs at the one-dimensional TPB line. The concept

'direct TPB reaction' may be first proposed by M.L. Liu, and several theoretical models by Liu's group have been developed to separate the contributions of the direct TPB reaction and the surface path [21, 39-41]. Recently, J. Laurencin et al developed an electrochemical model considering the parallel connection of surface path and direct TPB reaction [42]. They concluded that the contribution of direct TPB reaction could be significant depending on polarization and electrode microstructure. However, this concept has not yet been accepted widely. For example, S.B. Adler stated that 'when one begins to consider the specific chemical, electrochemical, and transport steps involved, one must abandon the idea of an ideal 1D geometric surface and consider the specific phases, surfaces, and interfaces involved in these steps.' [4]. Overall, evidence is essential to prove the existence of the direct TPB reaction. This is however still an open question today. Since the surface exchange has been well characterized by well-defined parameters, such as surface exchange coefficient and ASR, we just consider the surface exchange while bypassing the one-dimensional TPB reaction as a beginning point.

2.5 Gas diffusion within the pores

In addition to the transport of O^{2-} and e^- within MIEC bulk (Eqs. 14, 15) and surface exchange and charge transfer at MIEC surface and interface (Eqs. 30, 39, and 40), there exists diffusion of gaseous species within pores. Under typical working conditions of MIEC devices, the gas diffusion can be formulated by the Stefan-Maxwell equation, Knudsen equation, or Darcy equation. For MIEC devices such as solid oxide fuel cells, the thickness of porous electrodes is typically tens to hundreds of microns. When the current density is not very high, the gas diffusion within pores may be facile because the concentration polarization is usually not pronounced or even undetectable in the voltage vs. current curve [43].

2.6 Overpotentials of electron transport, oxygen ions transport and oxygen surface exchange

Overpotential, usually denoted by η is one of the most fundamental parameters, thus, should be clarified. In electrochemistry, the overpotential for example across a interface is defined by the change in the electrostatic (Galvani) potential drop across the interface when the interface is polarized away from equilibrium. Although, this definition is rigorous and clear, it encounters challenges in interpreting experimental data, since the electrostatic potential is immeasurable. In irreversible thermodynamics, the overpotential is the driving force that increases entropy, therefore produces Joule heat [22, 24]. The production rate of Joule heat per unit volume, $\dot{Q}$ [J/s/cm³] can be expressed as a product of absolute temperature, T and entropy production rate per unit volume, $\dot{s}$. In this work, the Joule heat is converted from the processes of electron transport, oxygen ion transport and oxygen surface exchange. Thus, we have,

$$\dot{Q} = T\dot{s} = -\sum_{e^-} J_{e^-} \nabla \tilde{\mu}_{e^-} - \sum_{O^{2-}} J_{O^{2-}} \nabla \tilde{\mu}_{O^{2-}} - \sum_{ORR} r_{O^{2-}}^{ORR} \frac{\mu_{O_2} - \mu_{O_2}^{pore}}{2\lambda} \tag{43}$$

Therein, J_{e^-}, $J_{O^{2-}}$ and $r_{O^{2-}}^{ORR}$ are the fluxes, and $-\nabla \tilde{\mu}_{e^-}$, $-\nabla \tilde{\mu}_{O^{2-}}$ and $-\left(\mu_{O_2} - \mu_{O_2}^{pore}\right)/2\lambda$ are the conjugate forces, respectively. λ represents the thickness of surface (or the side length of voxel in the following content). Using electric potential and chemical potential of O_2 instead of electrochemical potential of electrons and ions, Eq. 43 can be rewritten as,

$$\dot{Q} = -\sum_{e^-} J_{e^-} \nabla \left(-F\varphi\right) - \sum_{O^{2-}} J_{O^{2-}} \nabla \left(\frac{\mu_{O_2}}{2} - 2F\varphi\right) - \sum_{ORR} r_{O^{2-}}^{ORR} \frac{\mu_{O_2} - \mu_{O_2}^{pore}}{2\lambda} \tag{44}$$

The fluxes in Eq. 44 can be converted into current density by rearranging the Faraday constant. Thus, we have,

$$\dot{Q} = -\sum_{e^-} i_{e^-} \nabla (\varphi) - \sum_{O^{2-}} i_{O^{2-}} \nabla \left(\varphi - \frac{\mu_{O_2}}{4F} \right) - \sum_{ORR} i_{O^{2-}}^{ORR} \frac{\mu_{O_2} - \mu_{O_2}^{pore}}{4F\lambda} \tag{45}$$

Physically, the conjugate forces of current densities are the minus gradients of overpotentials. That is,

$$\dot{Q} = -\sum_{e^-} i_{e^-} \nabla \eta_{e^-} - \sum_{O^{2-}} i_{O^{2-}} \nabla \eta_{O^{2-}} - \sum_{ORR} i_{O^{2-}}^{ORR} \eta_{O^{2-}}^{ORR} / \lambda \tag{46}$$

Therefore, the overpotentials for electron transport, oxygen ions transport and oxygen surface exchange can be given by,

$$\eta_{e^-} = \varphi - \varphi_0 \tag{47}$$

$$\eta_{O^{2-}} = \left(\varphi - \varphi_0 \right) - \frac{\mu_{O_2} - \mu_{O_2}^0}{4F} \tag{48}$$

$$\eta_{O^{2-}}^{ORR} = \frac{\mu_{O_2} - \mu_{O_2}^{pore}}{4F} \tag{49}$$

where φ_0 and $\mu_{O_2}^0$ denote respectively the electric potential and chemical potential of O_2 at the reference coordinate. It is clear that the overpotentials are defined in 3D. It is also convenient to show their profiles along the thickness direction of the cell (the z axis), with $z = 0$ as the reference coordinate. On the cell level, η_{e^-} drives the electronic current in the internal and external circuits. When the electronic transport overpotentials at electrode/current collector interfaces are negligible, η_{e^-} denotes the output voltage; $\eta_{O^{2-}}$ drives the ionic current in the internal circuit. For SOFCs and SOECs, the chemical potentials of O_2 within the two electrodes just close to the current collector are (nearly) the same as those in the atmospheres. Thus, $\eta_{O^{2-}}$ is (nearly) the same as the difference between the output voltage and the Nernst potential, which is usually regarded as the overpotential of the cell; $\eta_{O^{2-}}^{ORR}$ drives the oxygen surface exchange and only has physical significance on the materials surface. It is the core concept for correlating oxygen surface exchange coefficient to AC impedance of a flat surface [4].

3. Numerical Methodology

By assuming that the charge transfer and gas diffusion are facile, the full model is formalized by Eqs. (14, 15, and 30). The objective of this section is to develop a numerical methodology to solve the coupling of Eqs. (14, 15, and 30) within the three-dimensional (3D) microstructure of MIEC devices, and eventually to obtain oxygen chemical potential, μ_{O_2} and electric potential, φ within the 3D microstructure. The calculation begins with the discretization of the 3D microstructure data. Typically, the 3D imaging techniques such as X-ray tomography and FIB serial sectioning generate 3D grey-level matrix in which the value of each voxel correlates to the local sample density and the side length of the voxel is approximately the spatial resolution. Then, image segmentation based primarily on grayscale contrast is usually used to label each voxel by an integer denoting a specific material phase. Thus, a 3D label matrix consisting of integers is obtained. This work employs the label matrix as the discretization data of the 3D microstructure. The label matrix is denoted by **M**. For convenience, the solid phases are denoted by 1, 2, ..., *N*, with *N* being the number of solid phases. The pore phase if any is divided into three classes. The physics fields are considered to be conducted along the thickness direction. Thus, the voxel value of the pores only percolating to the top layer of **M** is denoted by -1; the value of the pores only percolating to the bottom layer is -2; and the value of the isolated pores neither percolating to the top layer nor to the bottom layer is 0. By doing this, the physical properties of each voxel, including $\sigma_{O^{2-}}$, σ_{e^-} and $\mathfrak{R}_0^{ORR}$ of solid phase voxels and $\mu_{O_2}^{pore}$ of pore phase voxels and boundary conditions can be assembled easily. Then, voxels are considered as finite volume elements (FVEs). FVE method is used to calculate the averaged μ_{O_2} and φ of each voxel by applying Eqs. (14, 15, and 30) under boundary conditions. The coupling of differential

equations is actually discretized into linear algebraic equations using 3D matrix formalism, and solved by use of red-black ordering and successive over-relaxation [44] (refer to supporting materials). The algorithm is realized by a home-built Matlab function, by which the algebraic operations of 3D matrixes are quite convenient. The function inputs the label matrix of the 3D MIEC microstructure, electronic and ionic conductivities and surface exchange coefficient of oxygen for each sub-phase of the membrane (or qualities as a function of oxygen partial pressure), atmospheres at both the top side and bottom side of the membrane (e.g. oxygen partial pressure or oxygen chemical potential), electric potential applied on both the top side and bottom side of the membrane, over-relaxation factor, and termination criterion value of the iteration. The function outputs the 3D matrixes of oxygen chemical potential and electric potential, and their maximum relative errors as a function of iteration steps. Other Matlab functions are developed for the post-processing, including the calculations of ionic/electronic current density field, oxygen partial pressure field, averaged ionic/electronic current density and overpotentials across the thickness direction of MIEC membrane, area-specific resistance (ASR) of electrodes, oxygen permeation flux, voltage vs. current curve, and the 3D visualization of the electrochemical fields.

4. Results and discussion

Demonstrative calculations are performed for the three cases: 1) the LSM/YSZ/LSM and LSCF/YSZ/LSCF symmetric cells; 2) the GDC-GFO composite OSM membrane; and 3) the GDC-Ni/GDC/GDC-SSC SOFC/SOEC. The transport properties of materials are given in table 1 [45-54]. The experimental data for cases 2) and 3) is from our previous publications [46, 55, 56], where the experimental details are available. Considering the article length, the results and discussion of cases 1) and 2) are given in the supporting materials, which show the capability of resolving various MIEC systems with a broad range of transport properties operating under

various conditions and the capability of tackling a huge domain size. Case study 3) is presented in what follows. In addition to studying cell-level performance, emphasis will be given to studying the local distributions of electrochemical fields within the MIEC microstructures, and especially at the vicinity of surface and interface.
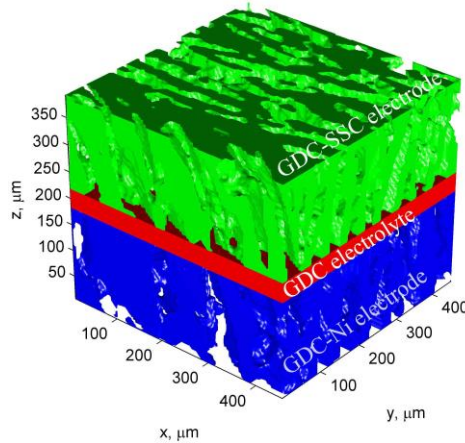

Figure 2. The three-dimensional microstructure of the GDC-Ni/GDC/GDC-SSC cell reconstructed by X-ray computed tomography with a spatial resolution of 4.5 μm.

The GDC-Ni/GDC/GDC-SSC cell with hierarchically porous electrode microstructure is fabricated, in our previous study, by freeze-drying tape-casting method and demonstrates a maximum power density of 0.65 W/cm^2 and long-term stability at 500 ^{o}C [46]. The high performance is attributed to the unique microstructural features of the electrodes, which has been reconstructed by a Micro-XCT400 instrument. Here, we calculate the distributions of the electrochemical fields and the cell performance with the 3D tomographic data of the cell. Fig. 2 shows a sub-domain of the 3D cell microstructure. As shown, the straight sheet pores with width of ~30 μm penetrate the electrodes, thus promoting gas diffusion within the electrode. The impedance analysis proves that the gas diffusion resistance is negligible compared to the electrode ASR. In addition, there also exist sub-micron pores percolating the electrode skeleton

that increases the TPB length and thus decreases the electrode ASR. However, the sub-micron pores, and differentiation of the solid phases, were not captured by the XCT in this work due to imaging with a voxel size of 4.5 μm. Although the Micro-XCT400 instrument, by using a higher magnification objective lens, can achieve better than 1 μm resolution, the somewhat coarser voxel resolution of 4.5 μm was utilized in this study to focus on the skeleton and sheet pores of electrodes and the GDC electrolyte. In addition, use of this lower level of magnification also permits a larger field of view, enabling reconstruction of a very large domain of the cell. This is important for robust calculation. The calculation is conducted for the cell operating at 500 °C. The transport properties of the composite electrodes are estimated by the properties of the individual components and the electrode ASR (Eq. 38). The oxygen partial pressure dependence of the electronic conductivity of GDC electrolyte is considered. Atmospheres of GDC-Ni fuel electrode and GDC-SSC air electrode are 3 vol.% H_2O - 97 vol.% H_2 and air, respectively.
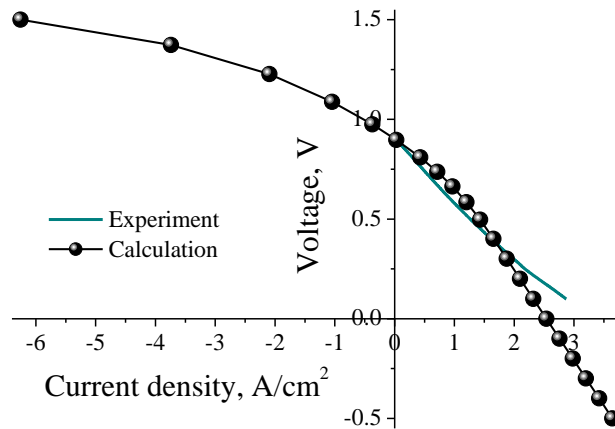
Figure 3. Calculation results of the cell voltage *vs.* cell output current density of the GDC-Ni/GDC/GDC-SSC button cell operated at 500 °C with the validation of experimental data. Atmospheres of GDC-Ni fuel electrode and GDC-SSC air electrode are 3 vol.% H_2O - 97 vol.% H_2 and air, respectively.

Fig. 3 shows the calculated voltage vs. current (V-I) curve of the cell and the experimental data. Depending on the voltage applied on the cell, the cell can operate in the SOFC mode (quadrant one of the V-I curve), the SOEC mode (quadrant two), or the driven-SOFC mode (quadrant four). In the SOFC mode, the imperfect fitting may be derived from the oxygen pressure dependence of the surface exchange coefficient, which is at this time not accessible and thus not considered by the calculation. The surface exchange coefficients here are the ones under open circuit condition. The surface exchange coefficients may increase by SOFC polarization, due to electrochemical activation. This could lead to a better fitting of the V-I curve. Indeed, a perfect fitting could be shown by tailoring the oxygen surface exchange coefficient for different output currents. But it is redundant without experimental study for the oxygen pressure dependence of the surface exchange coefficient. To our knowledge, little work on this topic is available in the literature. This is a new, growing and potentially important area of research in the field of fuel cells. Instead of showing a perfect fitting between the simulated V-I curve and the experimental V-I curve, we expect to explain some general yet important phenomenons that have not been clarified well by theoretical models, for instance the range of oxygen partial pressure distribution within the MIEC device and the stability of materials and interfaces under various polarization modes. When the cell shifts from the driven-SOFC mode to the SOFC mode and to the SOEC mode, the V-I response shows nonlinearity. This is attributed to the nonlinear relationship between the electronic conductivity of GDC and the oxygen partial pressure. The nonlinearity in the V-I curve is usually observed in the solid oxide cells based on doped ceria electrolyte [57, 58]. In what follows, we choose the three working points at voltages of 1.5 V, 0.5 V, and -0.5 V, which correspond respectively to the SOEC mode, SOFC mode, and driven-SOFC mode for discussion of the electrochemical fields within the cell. Fig. S16 shows the

convergence curves of relative errors for the three cases. The computational errors of electronic and ionic current densities are converged to sufficiently small levels compared to the current densities (Fig. S17), showing the calculation is well converged.
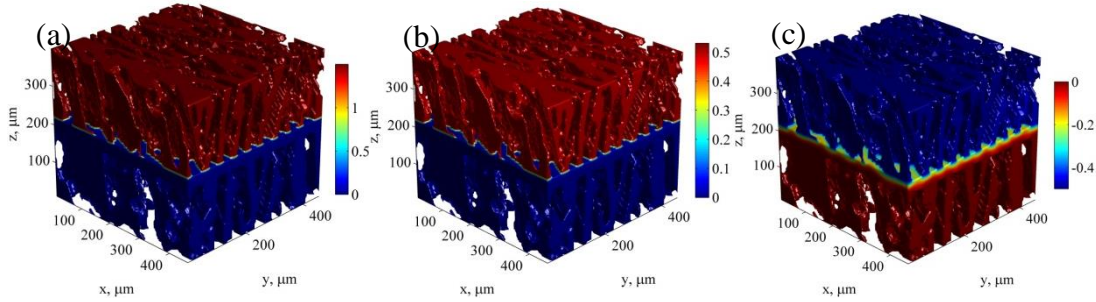

Figure 4. Electric potential distribution within the GDC-Ni/GDC/GDC-SSC button cell operated at 500 ^{o}C under cell voltage of 1.5 V (a), 0.5 V (b), and -0.5 V (c). Atmospheres of GDC-Ni anode and GDC-SSC cathode are 3 vol.% H_2O - 97 vol.% H_2 and air, respectively. Assembly of the cell is GDC-Ni anode/GDC electrolyte/GDC-SSC cathode along positive direction of Z axis.
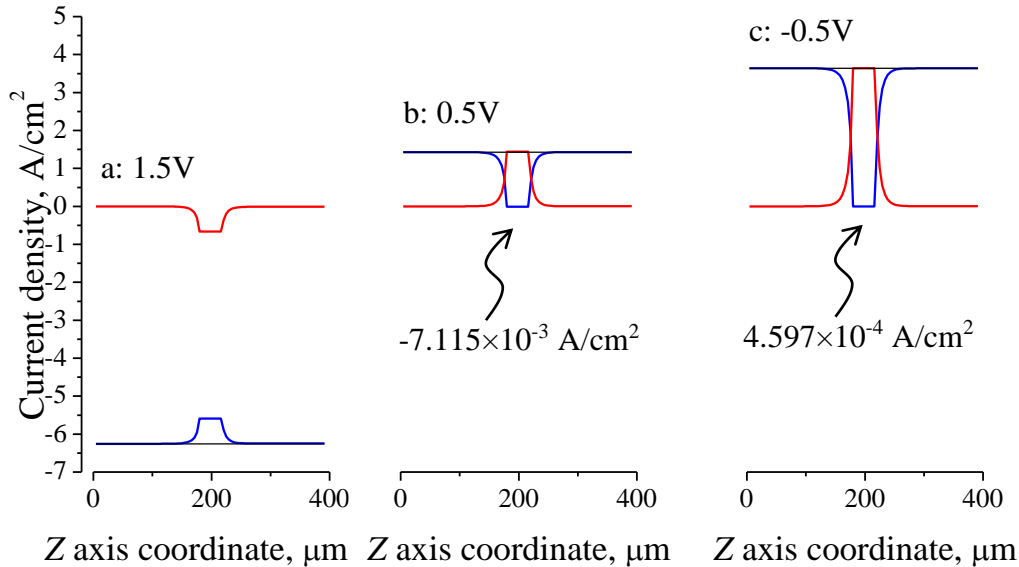
Figure 5. Averaged current densities of O^{2-} (red curve) and e^{-} (blue curve) and their summation (black curve) along *Z* axis direction of the GDC-Ni/GDC/GDC-SSC button cell. (a, b, and c) shows respectively the calculation results at cell voltages of 1.5 V, 0.5 V, and -0.5 V. The operation temperature is 500 °C. Atmospheres of GDC-Ni fuel electrode and GDC-SSC air electrode are 3 vol.% H_2O - 97 vol.% H_2 and air, respectively.

Fig. 4 shows the electric potential distribution within the cell. It is interesting to note that in the SOEC and the driven-SOFC mode, the electric potential within the cell is bounded by the values applied to the electrode boundaries. However in the SOFC mode, the electric potential within the cell lies out of the bounds of cell voltage. A rational interpretation for this phenomenon may be that the cell generates electricity power in the SOFC mode, but consumes electricity power in the SOEC mode and the driven-SOFC mode.
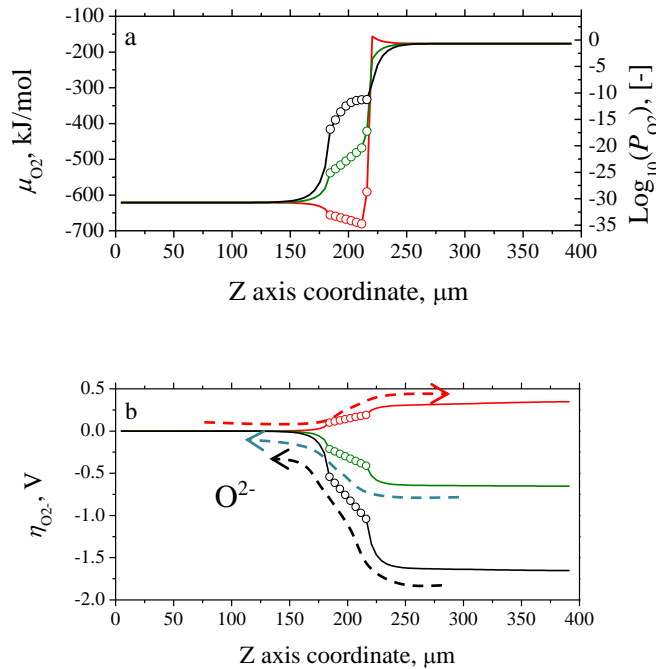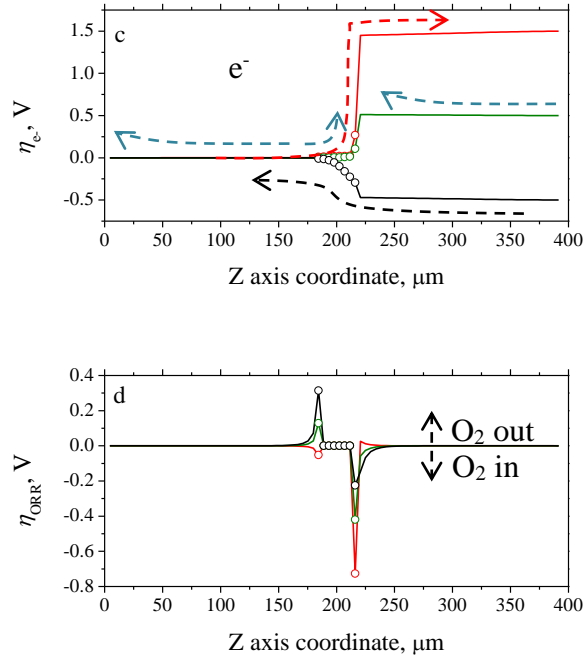
Figure 6. The distributions of oxygen chemical potential, logarithm of oxygen partial pressure (Log$_{10}P_{O2}$), overpotentials of ionic transport, electronic transport and oxygen surface exchange along the thickness direction (the Z-axis) of the GDC-Ni/GDC/GDC-SSC cell, under cell voltage of 1.5 V (red curve), 0.5 V (olive curve), and -0.5 V (black curve). The scatters represent the values in GDC electrolyte.

Fig. 5 shows the averaged ionic and electronic current densities across the cell for the SOEC, SOFC, and driven-SOFC modes. It is shown that, in the SOEC mode, both the electronic and ionic currents are negative. In other words, oxygen ions and electrons flow from the GDC-Ni electrode bottom surface (low oxygen partial pressure side) to the GDC-SSC electrode top surface (high oxygen partial pressure side). This is also shown by the monotonic increasing of the overpotentials of electronic and ionic transports from the GDC-Ni electrode bottom surface to the GDC-SSC electrode top surface (Fig. 6b and c). In the GDC-SSC electrode side, the high voltage reverses the direction of the ORR reaction, so that the external circuit captures the

31

electrons released by the reversed ORR reaction, as well as the electrons in the GDC-Ni fuel electrode via transport through the GDC electrolyte. In the SOFC mode, the ionic current is positive. But the electronic current changes signs at somewhere in the electrodes close to the electrolyte, indicating that the electrons consumed by ORR reaction at the GDC-SSC air electrode come from the GDC-Ni fuel electrode via the external circuit as well as the GDC electrolyte (the short-circuit current). This is also shown by the profile of electronic transport overpotential along the thickness direction (Fig. 6c). In the driven-SOFC mode, both the ionic and electronic currents are positive. That is, oxygen transports from the high oxygen partial pressure side to the low oxygen partial pressure side, but the electrons flowing into the GDC-SSC air electrode via external circuit exceed the demand of the ORR reaction, with the surplus electrons flowing to the GDC-Ni fuel electrode via GDC electrolyte.
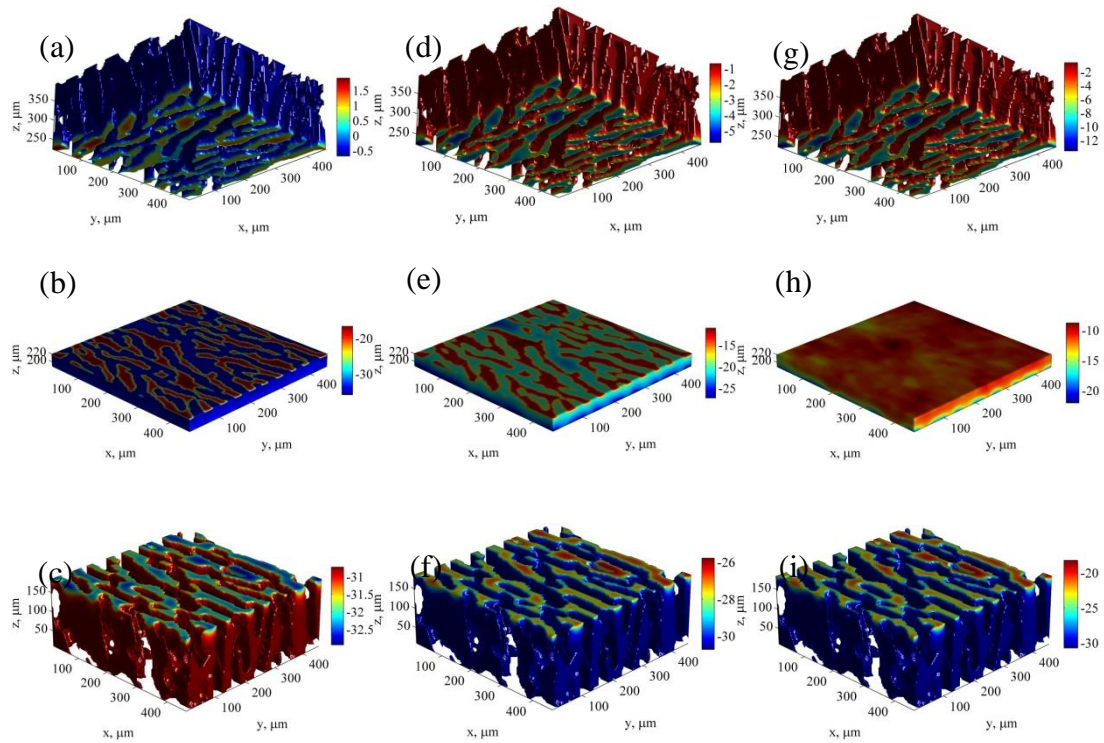
Figure 7. The spatial distributions of the logarithm of oxygen partial pressure ($Log_{10}P_{O2}$) within the GDC-Ni/GDC/GDC-SSC button cell at cell voltage of 1.5 V (a, b, c), 0.5 V (d, e, f), and -0.5 V (g, h, i). (a, d, g) show the GDC-SSC air electrode, (b, e, h) show the GDC electrolyte, and (c, f, i) show the GDC-Ni fuel electrode. The operation temperature is 500 °C. Atmospheres of GDC-Ni fuel electrode and GDC-SSC air electrode are 3 vol.% H_2O - 97 vol.% H_2 and air, respectively.

Fig. 7 shows the distribution of oxygen partial pressure within the cell in the SOEC, SOFC, and driven-SOFC modes. The distributions are visualized separately in the GDC-SSC electrode, GDC electrolyte, and GDC-Ni electrode, to check the status of electrode/electrolyte interface. It is shown that, the oxygen pressure lies out of the bounds of 0.21 atm at the GDC-SSC electrode atmosphere and 1.86×10^{-31} atm at the GDC-Ni electrode atmosphere. In the bulk of GDC-SSC electrode far away from the electrode/electrolyte interface (Fig. 7a), the oxygen pressure approaches to 0.21 atm in the atmosphere. However the high oxygen pressure in range of 10 ~ 100 atm is built up within a 10 μm thick region of the GDC-SSC electrode close to the electrode/electrolyte interface. This is a strong indicator that the GDC-SSC electrode may delaminate from the GDC electrolyte. While in the GDC electrolyte (Fig. 7b), the oxygen pressure lies in the range between 10^{-17} atm and 10^{-35} atm, out of the bounds by the atmospheres. Thus, the reduction of GDC electrolyte close to the GDC-Ni electrode may occur. The reason that high oxygen pressure has not built up in the electrolyte may be due to the electronic conduction of the GDC material. In the GDC-Ni electrode (Fig. 7c), the low oxygen pressure of 5.12×10^{-34} atm is built up close to the electrode/electrolyte interface, elsewhere approaches to 1.86×10^{-31} atm in the atmosphere. It is noted that the thermodynamic analysis by Virkar postulates that the oxygen pressure in the electrode is the same as the value in the atmosphere

[23]. The present analysis demonstrates that the high/low oxygen pressure can build up in the air/fuel electrode. Some experimental observations verify this conclusion. For example, the LSM air electrode delaminates from the YSZ electrolyte caused by the localized disintegration of the LSM grains close to the electrode/electrolyte interface, and the disintegration of LSM occurs initially at the central of the TPB rings [59], where the oxygen pressure is higher compared to the TPB regions, as shown in Fig. 7a. In the SOFC mode (Fig. 7d-f), oxygen pressure within the cell is bounded by the values at atmospheres. The gradients of oxygen pressure within the electrode are limited to the electrode/electrolyte interfaces, showing the electrochemical active regions. In this mode, the components of the cell function safely in the specific atmospheres. In the driven-SOFC mode (Fig. 7g-i), oxygen pressure within the cell is also bounded by the values at atmospheres. This result is however, contrary to the results that high oxygen pressure can develop at the air electrode/electrolyte interface in the driven-SOFC mode, and thus may result in delamination [60]. But the failure of the cell may be caused by the reduction of the air electrode or the oxidation of the fuel electrode in the driven-SOFC mode. As shown in Fig. 7g, the low oxygen pressure of $10^{-12} \sim 10^{-13}$ atm is built up in the GDC-SSC electrode close to the electrode/electrolyte interface (Fig. 7g), indicating a risk of reduction of SSC material. While in the GDC-Ni electrode as shown in Fig. 7i, a maximum oxygen pressure of 5.8×10^{-19} atm is developed, indicating a risk of oxidation of Ni. The same results are shown by the distributions of oxygen partial pressure along the thickness direction (Fig. 6a). The predictions for the failure modes driven by electrode potential are all in agreement with the reported observations [61]. The present framework provides new insights into the stability of the MIEC devices under the various working modes from a thermodynamic perspective.

Fig. 8 shows the linear profiles of oxygen pressure in the GDC-SSC electrode, GDC electrolyte, and GDC-Ni electrode just at the electrode/electrolyte interface, showing that the oxygen pressure is bounded by the values at atmospheres in the SOFC mode and driven-SOFC mode, but exceeds the bounds at atmospheres in the SOEC mode. In addition, it is interesting to note that, independent of the operation mode, the oxygen pressure in the GDC electrolyte just at the electrolyte surface exposing to the air electrode (GDC-SSC electrode) is always lower than the oxygen pressure in the atmosphere (0.21 atm). In other words, the GDC electrolyte surface exposing to the air electrode always operates in the fuel cell mode. This is validated by the corresponding profiles of ionic current density along direction z in the GDC electrolyte just at the electrolyte/air electrode interface (Fig. 8), and the distribution of overpotential of oxygen surface exchange along the thickness direction (Fig. 6d). It is shown that the direction of ionic current at the GDC-SSC electrode/GDC electrolyte interface depends on the operation mode, but the ionic current density at the GDC electrolyte surface is always positive, that is oxygen ions incorporates into the GDC electrolyte via the ORR reaction. This phenomenon may be due to the electronic conduction of the GDC electrolyte. While for the YSZ electrolyte, whose electronic conductivity is relatively low, the YSZ electrolyte surface operates in the SOEC mode when the cell operates in the SOEC mode (Fig. S6).

Overall, the performance and stability of the GDC-Ni/GDC/GDC-SSC cell in various operation modes can be analyzed by the present framework in a great detail. The electrochemical fields such as electric potential, oxygen partial pressure, ionic and electronic current densities within the 3D cell microstructure, especially near the regions at electrode/electrolyte interface demonstrate critical roles in determining the cell performance and stability.
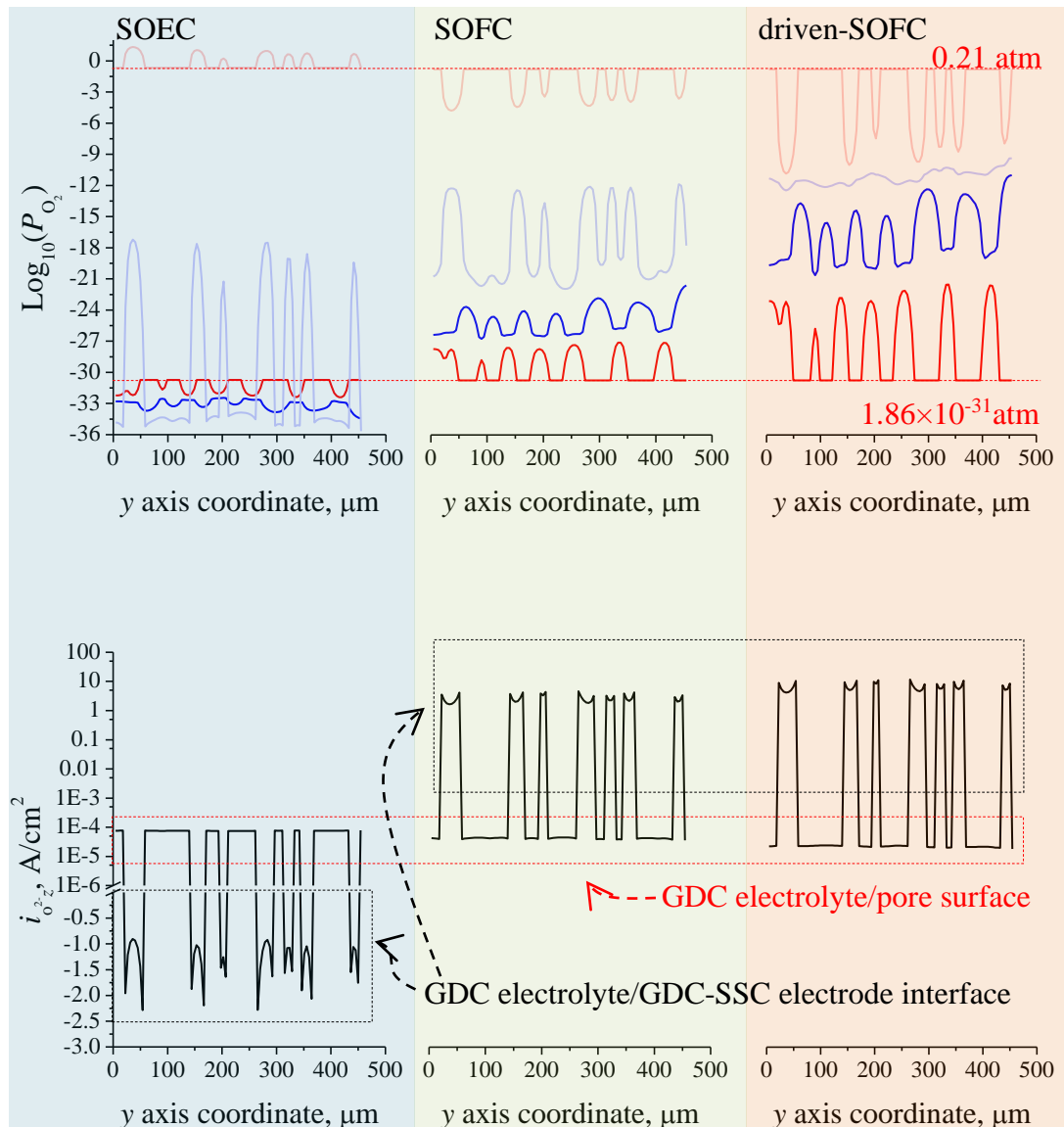
Figure 8. The profiles of the logarithm of oxygen partial pressure ($Log_{10}P_{O2}$) within the electrolyte (black curves) and electrodes (red curves) just at electrolyte/electrode interface, and the ionic current along positive direction of z axis (i_{O2-z}) within the electrolyte just at the electrolyte/GDC-SSC electrode interface, when the GDC-Ni/GDC/GDC-SSC button cell operates at SOEC, SOFC, and driven SOFC modes. For the profiles of $Log_{10}P_{O2}$, the light/heavy red curve denotes the profile within the GDC-SSC/GDC-Ni electrode. The light/heavy blue

curve denotes the profile within the GDC electrolyte adjacent to the GDC-SSC/GDC-Ni electrode.

5. Conclusions

The steady-state thermodynamics framework conforming to local equilibrium postulation is capable of correlating the fundamental properties of MIEC materials (ionic and electronic conductivity and surface exchange coefficient) and the 3D microstructure of the MIEC membrane device to its performance and stability. Case studies for the LSM/YSZ/LSM and LSCF/YSZ/LSCF symmetric cells, GDC-CFO OXM membrane, and GDC-Ni/GDC/GDC-SSC SOFC/SOEC verify the calculation results, consolidate classic understanding and provide new insight into the correlation between local electrochemical field distributions and performance and stability of the MIEC membranes. The present framework is capable of considering the dependence of the transport properties on the oxygen partial pressure, and capable of adding charge transfer across interface and gas diffusion within pores. The calculation of defect concentration is straightforward by considering the defect chemistry of the MIECs. Based on this framework, it is feasible to design advanced microstructures of the MIEC devices with enhanced performance and stability by using topology optimization, which is in progress.

References

[1] Z. Shao, W. Zhou, Z. Zhu, Advanced synthesis of materials for intermediate-temperature solid oxide fuel cells, Prog. Mater. Sci. 57 (2012) 804-874.

[2] M. Ni, M.K.H. Leung, D.Y.C. Leung, Technological development of hydrogen production by solid oxide electrolyzer cell (SOEC), Int. J. Hydrogen Energy 33 (2008) 2337-2354.

[3] J. Sunarso, S. Baumann, J.M. Serra, W.A. Meulenberg, S. Liu, Y.S. Lin, J.C. Diniz da Costa, Mixed ionic-electronic conducting (MIEC) ceramic-based membranes for oxygen separation, J. Membrane Sci. 320 (2008) 13-41.

[4] S.B. Adler, Factors governing oxygen reduction in solid oxide fuel cell cathodes, Chem. Rev. 104 (2004) 4791-4844.

[5] S.B. Adler, J.A. Lane, B.C.H. Steele, Electrode kinetics of porous mixed-conducting oxygen electrodes, J. Electrochem. Soc. 143 (1996) 3554-3564.

[6] C.W. Tanner, K. Fung, A.V. Virkar, The effect of porous composite electrode structure on solid oxide fuel cell performance: I. Theoretical Analysis, J. Electrochem. Soc. 144 (1997) 21-30.

[7] M. Shah, J.D. Nicholas, S.A. Barnett, Prediction of infiltrated solid oxide fuel cell cathode polarization resistance, Electrochem. Commun. 11 (2009) 2-5.

[8] M. Ni, M.K.H. Leung, D.Y.C. Leung, Micro-scale modelling of solid oxide fuel cells with micro-structurally graded electrodes, J. Power Sources 168 (2007) 369-378.

[9] H. Zhu, R.J. Kee, V.M. Janardhanan, O. Deutschmann, D.G. Goodwin, Modeling elementary heterogeneous chemistry and electrochemistry in solid-oxide fuel cells, J. Electrochem. Soc. 152 (2005) A2427-A2440.

[10] S.H. Chan, X.J. Chen, K.A. Khor, Cathode micromodel of solid oxide fuel cell, J. Electrochem. Soc. 151 (2004) A164-A172.

[11] K.L. Duncan, E.D. Wachsman, Continuum-level analytical model for solid oxide fuel cells with mixed conducting electrolytes fuel cells and energy conversion, J. Electrochem. Soc. 156 (2009) B1030-1038.

[12] W.C. Chueh, S.M. Haile, Electrochemistry of mixed oxygen ion and electron conducting electrodes in solid electrolyte cells, Annu. Rev. Chem. Bionol. Eng. 3 (2012) 313-341.

[13] A. P. Cocco, G. J. Nelson, W. M. Harris, A. Nakajo, J. J. Lombardo, T. D. Myles, A. M. Kiss, W. K. S. Chiu, Three-dimensional microstructural imaging methods for energy materials, Phys. Chem. Chem. Phys. 15 (2013) 16377-16407.

[14] P.R. Shearing, Q. Cai, J.I. Golbert, V. Yufit, C.S. Adjiman, N.P. Brandon, Microstructural analysis of a solid oxide fuel cell anode using focused ion beam techniques coupled with electrochemical simulation, J. Power Sources, 195 (2010) 4804-4810.

[15] K.N. Grew, Y.S. Chu, J. Yi, A.A. Peracchio, J.R. Izzo, Y. Hwu, F. De Carlo, W.K.S. Chiu, Nondestructive nanoscale 3D elemental mapping and analysis of a solid oxide fuel cell anode, J. Electrochem. Soc. 157 (2010) B783-B792.

[16] N. Shikazono, D. Kanno, K. Matsuzaki, H. Teshima, S. Sumino, N. Kasagi, Numerical assessment of SOFC anode polarization based on three-dimensional model microstructure reconstructed from FIB-SEM images, J. Electrochem. Soc. 157 (2010) B665-B672.

[17] B. Rüger, A. Weber, E. Ivers-Tiffée, 3D-modelling and performance evaluation of mixed conducting (MIEC) cathodes, ECS Trans. 7 (2007) 2065-2074.

[18] A. Häffelin, J. Joos, M. Ender, A. Weber, E. Ivers-Tiffée, Time-dependent 3D impedance model of mixed-conducting solid oxide fuel cell cathodes, J. Electrochem. Soc. 160 (2013) F867-F876.

[19] T. Carraro, J. Joos, B. Rüger, A. Weber, E. Ivers-Tiffée, 3D finite element model for reconstructed mixed-conducting cathodes: I. Performance quantification, Electrochim. Acta 77 (2012) 315-323.

[20] T. Carraro, J. Joos, B. Rüger, A. Weber, E. Ivers-Tiffée, 3D finite element model for reconstructed mixed-conducting cathodes: II. Parameter sensitivity analysis, Electrochim. Acta 77 (2012) 309-314.

[21] M.E. Lynch, D. Ding, W.M. Harris, J.J. Lombardo, G.J. Nelson, W.K.S. Chiu, M. Liu, Flexible multiphysics simulation of porous electrodes: Conformal to 3D reconstructed microstructures, Nano Energy, 2 (2013) 105-115.

[22] A.V. Virkar, Theoretical analysis of the role of interfaces in transport through oxygen ion and electron conducting membranes, J. Power Sources 147 (2005) 8-31.

[23] A.V. Virkar, Mechanism of oxygen electrode delamination in solid oxide electrolyzer cells, Int. J. Hydrogen Energy 35 (2010) 9527-9543.

[24] N.W. Tschoegl, 23 - The postulates of steady-state thermodynamics, in: Fundamentals of Equilibrium and Steady-State Thermodynamics, Elsevier Science, Amsterdam, 2000, pp. 178-181.

[25] G.E. Murch, Diffusion Kinetics in Solids, in: Phase Transformations in Materials, Wiley-VCH Verlag GmbH & Co. KGaA, 2005, pp. 171-238.

[26] A.R. Allnatt, Einstein and linear response formulae for the phenomenological coefficients for isothermal matter transport in solids, J. Phys. C: Solid State Phys. 15 (1982) 5605-5613.

[27] A.J. Bard, L.R. Faulkner, Electrochemical Methods: Fundamentals and Applications, 2nd ed., John Wiley & Sons, New York, 2002.

[28] M.H. Hebb, Electrical conductivity of silver sulfide, J. Chem. Phys. 20 (1952) 185.

[29] R.J. Kee, H. Zhu, B.W. Hildenbrand, E. Vøllestad, M.D. Sanders, R.P. O'Hayre, Modeling the steady-state and transient response of polarized and non-polarized proton-conducting doped-perovskite membranes, J. Electrochem. Soc. 160 (2013) F290-F300.

[30] G.E. Murch, J.C. Dyre, Correlation effects in tracer diffusion and ionic conductivity, Solid State Ionics 20 (1986) 203-207.

[31] N.W. Tschoegl, 20 - Chemical reactions, in: Fundamentals of Equilibrium and Steady-State Thermodynamics, Elsevier Science, Amsterdam, 2000, pp. 154-159.

[32] M.Z. Bazant, Theory of chemical kinetics and charge transfer based on nonequilibrium thermodynamics, Accounts Chem. Res. 46 (2012) 1144-1160.

[33] R. Merkle, J. Maier, How is oxygen incorporated into oxides? A comprehensive kinetic study of a simple solid-state reaction with $SrTiO_3$ as a model material, Angewandte Chemie International Edition, 47 (2008) 3874-3894.

[34] J.E. ten Elshof, M.H.R. Lankhorst, H.J.M. Bouwmeester, Oxygen exchange and diffusion coefficients of strontium-doped lanthanum ferrites by electrical conductivity relaxation, J. Electrochem. Soc. 144 (1997) 1060-1067.

[35] J. Claus, M. Leonhardt, J. Maier, Tracer diffusion and chemical diffusion of oxygen in acceptor doped $SrTiO_3$, J. Phys. Chem. Solids 61 (2000) 1199-1207.

[36] Y. Zhang, Y. Chen, M. Yan, F. Chen, Reconstruction of relaxation time distribution from linear electrochemical impedance spectroscopy, J. Power Sources 283 (2015) 464-477.

[37] M. Liu, Distributions of charged defects in mixed ionic-electronic conductors: I. general equations for homogeneous mixed ionic-electronic conductors, J. Electrochem. Soc. 144 (1997) 1813-1834.

[38] R. Radhakrishnan, A.V. Virkar, S.C. Singhal, Estimation of charge-transfer resistivity of $La_{0.8}Sr_{0.2}MnO_3$ cathode on $Y_{0.16}Zr_{0.84}O_2$ electrolyte using patterned electrodes, J. Electrochem. Soc. 152 (2005) A210-A218.

[39] M. Liu, Equivalent circuit approximation to porous mixed-conducting oxygen electrodes in solid-state cells, J. Electrochem. Soc. 145 (1998) 142-154.

[40] M.L. Liu, Z. Wu, Significance of interfaces in solid-state cells with porous electrodes of mixed ionic–electronic conductors, Solid State Ionics 107 (1998) 105–110.

[41] M.E. Lynch, DS. Mebane, Y. Liu, M.L. Liu, Triple-phase boundary and surface transport in mixed conducting patterned electrodes, J. Electrochem. Soc. 155 (2008) B635-B643.

[42] J. Laurencin, M. Hubert, K. Couturier, T. Le Bihan, P. Cloetens, F. Lefebvre-Joud, E. Siebert, Reactive mechanisms of LSCF single-phase and LSCF-CGO composite electrodes operated in anodic and cathodic polarisations, Electrochim. Acta 174 (2015) 1299–1316.

[43] F. Zhao, A.V. Virkar, Dependence of polarization in anode-supported solid oxide fuel cells on various cell parameters, J. Power Sources 141 (2005) 79-95.

[44] C.T. Kelley, 1. Basic Concepts and Stationary Iterative Methods, in: Iterative Methods for Linear and Nonlinear Equations, SIAM, Philadelphia, 1995, pp. 3-10.

[45] H. Takamura, M. Kawai, K. Okumura, A. Kamegawa, M. Okada, Preparation and oxygen permeability of Gd-Doped Ceria and spinel-type ferrite composites, MRS Proceedings, 756 (2002) EE8.11.11-16.

[46] Y. Chen, Y. Lin, Y. Zhang, S. Wang, D. Su, Z. Yang, M. Han, F. Chen, Low temperature solid oxide fuel cells with hierarchically porous cathode nano-network, Nano Energy 8 (2014) 25-33.

[47] Y. Ji, J.A. Kilner, M.F. Carolan, Electrical properties and oxygen diffusion in yttria-stabilised zirconia (YSZ)-La$_{0.8}$Sr$_{0.2}$MnO$_{3-d}$ (LSM) composites, Solid State Ionics 176 (2005) 937-943.

[48] R.A. De Souza, J.A. Kilner, Oxygen transport in La$_{1-x}$Sr$_x$Mn$_{1-y}$Co$_y$O$_{3-d}$ perovskites: Part I. Oxygen tracer diffusion, Solid State Ionics 106 (1998) 175-187.

[49] L. Zhu, L. Zhang, A.V. Virkar, Measurement of ionic and electronic conductivities of yttria-stabilized zirconia by an embedded electrode method, J. Electrochem. Soc. 162 (2015) F298-F309.

[50] J.A. Lane, S.J. Benson, D. Waller, J.A. Kilner, Oxygen transport in La$_{0.6}$Sr$_{0.4}$Co$_{0.2}$Fe$_{0.8}$O$_{3-d}$, Solid State Ionics 121 (1999) 201-208.

[51] H.J.M. Bouwmeester, H. Kruidhof, A.J. Burggraaf, Importance of the surface exchange kinetics as rate limiting step in oxygen permeation through mixed-conducting oxides, Solid State Ionics 72 (1994) 185-194.

[52] S. Lübke, H.D. Wiemhöfer, Electronic conductivity of Gd-doped ceria with additional Pr-doping, Solid State Ionics 117 (1999) 229-243.

[53] J. H. Park, R. Blumenthal, Electronic transport in 8 mole percent Y_2O_3-ZrO_2, J. Electrochem. Soc. 136 (1989) 2867-2876.

[54] S.W. Zha, C.R. Xia, G.Y. Meng, Calculation of the e.m.f. of solid oxide fuel cells, J. Appl. Electrochem. 31 (2001) 93-98.

[55] Y. Lin, S. Fang, D. Su, K.S. Brinkman, F. Chen, Enhancing grain boundary ionic conductivity in mixed ionic-electronic conductors, Nat. Commun. 6 (2015).

[56] W.M. Harris, K.S. Brinkman, Y. Lin, D. Su, A.P. Cocco, A. Nakajo, M.B. DeGostin, Y.-c.K. Chen-Wiegart, J. Wang, F. Chen, Y.S. Chu, W.K.S. Chiu, Characterization of 3D interconnected microstructural network in mixed ionic and electronic conducting ceramic composites, Nanoscale 6 (2014) 4480-4485.

[57] C. Gaudillere, L. Navarrete, J.M. Serra, Syngas production at intermediate temperature through H_2O and CO_2 electrolysis with a Cu-based solid oxide electrolyzer cell, Int. J. Hydrogen Energy 39 (2014) 3047-3054.

[58] A. Mahmood, S. Bano, J.H. Yu, K.H. Lee, High-performance solid oxide electrolysis cell based on ScSZ/GDC (scandia-stabilized zirconia/gadolinium-doped ceria) bi-layered electrolyte and LSCF (lanthanum strontium cobalt ferrite) oxygen electrode, Energy 90 (2015) 344-350.

[59] K. Chen, S.P. Jiang, Failure mechanism of $(La,Sr)MnO_3$ oxygen electrodes of solid oxide electrolysis cells, Int. J. Hydrogen Energy 36 (2011) 10541-10549.

[60] A.V. Virkar, A model for solid oxide fuel cell (SOFC) stack degradation, J Power Sources 172 (2007) 713-724.

[61] J.T.S. Irvine, D. Neagu, M.C. Verbraeken, C. Chatzichristodoulou, C. Graves, M.B. Mogensen, Evolution of the electrochemical interface in high-temperature fuel cells and electrolysers, Nature Energy 1 (2016) 15014.